EMS Engineering Science Journal

Research Article

Production of 3D Printed Scale Models from Microscope Volume Datasets for use in STEM Education

Perry I[1], Szeto J-Y[1], Isaacs MD[1], Gealy EC[1], Rose R[1], Scofield S[1], Watson PD[1], Hayes AJ[1*]

[1]*Bioimaging Research Hub, Cardiff School of Biosciences, Cardiff University, Cardiff CF10 3AX. Wales, UK*

*Corresponding author: Dr. Anthony J. Hayes, Bioimaging Research Hub, Cardiff School of Biosciences, Cardiff University, Cardiff CF10 3AX, Wales, UK,
Tel: +44(0)2920876611;
Email: hayesaj@cardiff.ac.uk

Received: 19-06-2017
Accepted: 20-06-2017
Published: 21-07-2017

Abstract

Understanding the three-dimensional morphology of a biological sample at the microscopic level is a prerequisite to a functional understanding of cell biology, tissue development and growth. Images of microscopic samples obtained by compound light microscopy are customarily recorded and represented in two dimensions from a single orientation making it difficult to extrapolate 3D context from the 2D information. The commercialisation of fast, laser-based microscope systems (e.g. confocal, multi-photon or lightsheet microscopy) capable of generating volume datasets of microscopic samples through optical sectioning, coupled with advances in computer technology allowing accurate volume rendering of these datasets, have facilitated significant improvement in our 3D understanding of the microscopic world in virtual space. The advent of affordable 3D printing technology now offers the prospect of generating morphologically accurate, physical models from these microscope volume datasets for use in science education, outreach and engagement. 3D printed scale replicas will provide improved sensory perception, offering tactile as well as visual interaction, leading to improved understanding of structure function relationships. Here we present a technique to reliably generate detailed, physical 3D models from Z-stacks of optical sections from confocal and lightsheet microscopes using affordable, entry-level 3D printing technology. We use the technique to generate 3D printed models of a variety of different biological samples at a range of scales including pollen grains from two species of plant; blood cells from both human and earthworm species, a section of plant root; the compound eye of an ant; and a developing Zebrafish larva; all of which have been used in our teaching, engagement and outreach activities. Our methods can, in principle, be used to generate 3D printed models from microscope volume datasets of any small fluorescent or reflective samples.

Keywords: Confocal Microscopy; Lightsheet Microscopy; 3D Reconstruction; 3D Printing; STEM; Kinaesthetic Learning

Introduction

3D printing or "additive manufacturing" has evolved significantly as a transformative technology in recent years with dramatic improvements in printing speed, resolution and cost. There are now a variety of different 3D printing formats (e.g. stereolithography; SLA; selective laser sintering; SLS; fused filament fabrication, FFF) and printing materials (e.g. resin, plastic, metal), each with their own advantages and disadvantages [1,2] . These technologies have been widely exploited within a medical context to allow 3D conceptualisation of complex anatomic structures from computed tomography (CT), positron emission tomography (PET) or magnetic resonance (MR) scans and to generate implants and prosthetics in fields such as orthopaedics, spinal surgery and maxillofacial surgery (reviewed by [3,4]). 3D printing has also been used to generate models of organs (e.g. [5], biomolecules (e.g. [6] and crystal structures (e.g. [7]) as resources for research and teaching applications. The potential of the technology to convey meaningful 3D information at the microscopic level is also slowly becoming realised, with a handful of recent studies describing approaches for the creation of physical mod-

els from volume datasets obtained by both light microscopy [8-11], and electron microscopy [12-14]. The majority of these studies have utilised fused filament fabrication (FFF), which is one of the most common and cost-effective 3D printing methods in which a thermoplastic filament, usually either polylactic acid (PLA) or acrylonitrile butadiene styrene (ABS), is melted and extruded from a print head onto a heated support bed, thus building up the 3D print on a layer-by-layer basis – the resolution of the print being determined by the thickness of the printed layer.

In this study, we present a workflow to quickly and reliably generate scale replica 3D models of biological samples from volume datasets obtained by confocal and lightsheet microscopy, utilising both fluorescence (autofluorescence and targeted fluorochromes) and reflectance-based imaging modalities.The 3D printed models we have generated include samples from both plant and animal species and range in scale from the level of cell organelle to multicellular developmental organism, revealing both internal and external structure. The workflow and procedures we describe are, in principle, compatible with all imaging modalities that generate volume datasets by optical sectioning (e.g. deconvolved widefield microscopy, spinning disc microscopy, multi-photon microscopy etc) and thus can be applied to a variety of microscopy platforms and image processing and analysis software. The 3D prints we have produced have been utilised extensively and proven extremely successful in our STEM (science, technology, engineering and math) activities, science education, and outreach and engagement programmes.

Materials and Methods

The typical workflow for the methodology described below is depicted in Figure 1.

Samples

To evaluate the methodology, a range of different biological samples from single cells to multicellular organisms, including both plant and animal species, were imaged using confocal or lightsheet microscopy. Images were generated from cell/tissue autofluorescence, targeted fluorochromes and via confocal reflectance. The following samples were utilised:(1) Commercial unstained slide preparations of (a) pollen grains from the common Daisy (Bellis perennis) and Bulrush (Typha latifolia); (b) erythrocytes from a human blood cell smear; (c) a transverse section of root from the Lilly of the valley plant (Convallaria majalis). (2) suspensions of live, unlabelled leukocytes (coelomocytes) obtained from the coelomic cavity of the common earthworm (Eisenia fetida) by electrical extrusion; (3) a compound eye from the common garden ant (Myrmica rubra) sputter-coated with gold for confocal reflectance, and (4) a larval form of the Zebrafish (Danio rerio) at one day post-fertilisation (1 dpf) fluorescently labelled for both actin and cell nuclei (further details below). All image acquisition and 3D reconstruction was carried out in-house at the Bioimaging Research Hub at Cardiff School of Biosciences.

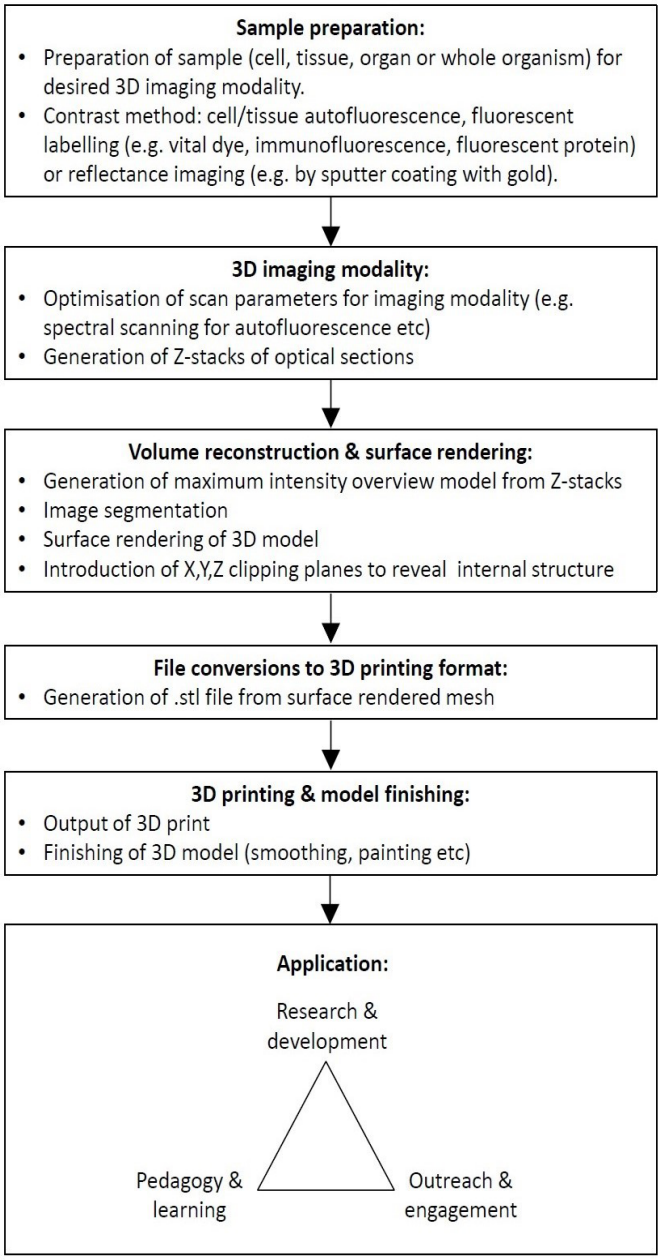

Figure 1. Schematic showing workflow involved in the generation of a 3D print from a microscope volume dataset.

Image Acquisition

Confocal Microscopy

Apart from the Zebrafish larva, which was imaged by lightsheet microscopy (see below), all other samples were imaged by confocal microscopy using sample autofluorescence to generate the 3D model. The ant compound eye sample was, in addition, imaged by confocal reflectance after physical vapour deposition with gold using standard scanning electron microscopic procedures. Confocal microscopy of the samples was performed using either a Leica TCS SP2 confocal (Leica,

Heidelberg, Germany) or a Zeiss LSM880 Airyscan confocal system (Zeiss, Jena, Germany). Individual samples were visualised using an objective lens appropriate to the physical dimensions of the specimen (refer to table 1). Scan parameters were optimised to record autofluorescent emissions derived from each sample using spectral (lambda, wavelength) scans to establish confocal detection bandwidths. For spectral scans, samples were excited typically at 405nm and emissions collected sequentially across the visible range and into the far red. Plots of fluorescent intensity against wavelength were then used to identify emission peaks (Figure 2A,B) and thus inform appropriate scan parameters (refer to table 1). Z-stacks of digital optical sections (typical image size of 512 x 512 pixels) were then taken through the specimen volume applying Nyquist sampling criteria and a pinhole size of 1 Airy unit (AU) to give the best signal to noise ratio. Line averaging was used for electronic noise reduction throughout. Datasets of confocal Z-stacks were saved in either .lei (Leica confocal software) or .czi (Carl Zeiss Image) formats.

Sample (contrast)	System	Objective	Laser line (nm)	Detection bandwidth (nm)
Daisy pollen (autofluorescence)	LSM880 & SP2	63x/1.4 oil	488 + 594	500-700nm
Bulrush pollen (autofluorescence)	LSM880	63x/1.4 oil	488 + 594	500-700nm
Erythrocyte (autofluorescence)	LSM880	63x/1.4 oil	514	500-700nm
Compound eye (autofluorescence/ reflectance)	SP2	10x/0.30	405 (fluorescence) 488 (reflectance)	420-480 (fluorescence) 485-490 (reflectance)
Root section (autofluorescence)	LSM880	63x/1.4 oil	488	500-600
Zebrafish larva (FITC-phalloidin: actin; DAPI: nuclei)	Lightsheet Z.1	20x/1.0	405 + 488	<550 (DAPI) >595 (FITC)

Table 1: Scan parameters used for Imaging Samples
FITC, fluorescein isothiocyanate; DAPI, 4',6-diamidino-2-phenylindole

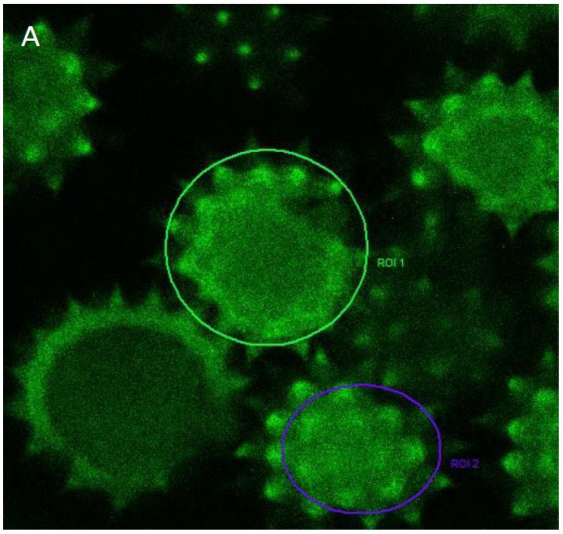

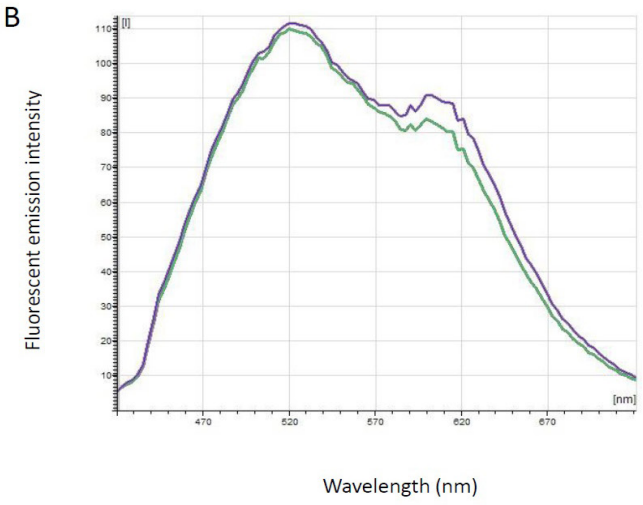

Figure 2. A. Spectral (wavelength, lambda) scan of autofluorescent emissions from Daisy pollen (Bellis perenis). Samples were excited with a 405nm laser and autofluorescent emissions collected from 415nm to 715nm.

B. Spectral plots of wavelength (nm) versus fluorescent emission intensity for regions of interest (ROIs) identified in A. Note emission peaks at 520nm and 620nm. Pollen grains were subsequently excited at 488nm and 594nm to optimise the signal from these emission peaks.

Lightsheet Microscopy

Lightsheet microscopy, performed using a Zeiss Lightsheet Z.1 system (Zeiss, Jena, Germany), was utilised for whole organism imaging. Zebrafish larvae (1 dpf) were fixed in 4% paraformaldehyde, washed and then fluorescently labelled overnight with FITC-phalloidin (10 microgrammes/ml; ThermoFisher Scientific) to stain filamentous actin. After washing, larvae were counter-stained with DAPI (0.5 microgrammes/ml; ThermoFisher Scientific) to selectively contrast the cell nuclei of the fish. Larvae were immersed in low melting point agarose, drawn into a warmed capillary tube and then loaded into the specimen chamber of a Zeiss Lightsheet Z.1 microscope [15]. The chamber was flooded with 0.1M PBS (pH7.4) and the extruded sample imaged using a x10 detection objective and x5 illumination objectives with appropriate excitation and emission settings for simultaneous recording of both DAPI (Ex max: 358nm; Em max: 461nm) and FITC (Ex max: 496nm; Em max: 516nm). A Z-stack, comprising 1650 optical sections (1920 x 1920 pixels) was taken through the whole organism using Nyquist sampling criteria. Datasets were output in the .czi file format.

Volume Reconstruction and Surface Rendering

Datasets from both confocal and lightsheet microscopes were opened in Bitplane Imaris for Cell Biologists version 8 (Oxford Instruments). Z-stacks of optical sections from each sample were 3D reconstructed using a maximum intensity algorithm to visualise both internal and external structure (this visualisation method projects the brightest voxels of the Z-stack in the image plane). The 3D models were then surface rendered via absolute intensity thresholding with smoothing and exported in the .vrml2 (Virtual Reality Modelling Language 2) file format. These files were imported into MeshLab (http://www.meshlab.net/), which is a free, open source software platform that provides additional editing tools to prepare the mesh models for 3D printing. The resultant surface rendered meshes were then exported in the .stl (STereoLithography) file format for 3D printing. N.B. the free, open source image processing software, Fiji (https://fiji.sc/; [20]) also provides an advanced toolset that will allow generation of .stl files from surface-rendered Z-series from all major microscopy platforms.

3D Printing and Processing

3D printing was performed using a Zortrax M200 3D printer, which is an affordable, entry-level FFF single colour 3D printer with a printing resolution of 90-400 microns (Zortrax; https://zortrax.com/printers/zortrax-m200/). For 3D printing, the .stl files generated in MeshLab were opened in Zortrax Z-Suite v1.7.1 software, re-sized and re-oriented with respect to the heated print bed (work field of 200x200x180mm). Models were prepared for printing in the Z-Suite software applying a typical print resolution of 140 microns with low infill, which provided a good compromise between resolution and speed. The 3D printer file (.Zcode format) was then printed overnight. Once each print was complete, the 3D output was removed from the printer and the external supporting scaffold carefully detached from the model using needle nose pliers, fine forceps and a scalpel. Larger digital models that were outside the print bed parameters (e.g. the Zebrafish larva) were cut using the Z-Suite 'Split' feature and printed as separate halves. The complementary halves were then fused together using a mixture of melted ABS in acetone and cyanoacrylate adhesive. Where necessary, any finishing (e.g. smoothing of edges from support stubble) was performed using a paint brush dipped in acetone. A water-based acrylic paint was used to contrast features of interest in the 3D print.

Results

Plant Pollen

Epifluorescence observation of pollen grains from the common daisy (Bellis perennis) and Bulrush (Typha latifolia) plants showed that both species were highly autofluorescent across the visible spectrum (Figures 2, 3 & 4; [16,17]). Confocal Z-stacks through individual grains provided striking morphological detail of both internal and external structure (Figure 3A-F, 4A-C). Maximum intensity 3D reconstructions provided volume overviews of the pollen grains and demonstrated an equivalent spherical diameter of approximately 30-35 micrometres in both species (Figure 3G & 4D). Bellis grains were spheroidal in morphology with prominent spiny ornamentation of their exine outer wall (Figure 3A-G), whereas Typha grains were grouped into tetrads, with reticulate patterning of their exine (Figure 4A-D). Surface rendering showed further topographic detail of the surface ornamentation of both species (Figures 3H & 4E and supplemental movie). Introduction of a clipping plane into the 3D model (Figure 3I) and image segmentation of greyscale values also allowed the underlying surfaces to be rendered in 3D (Figure 3J). Processing of surface rendered datasets for 3D printing resulted in .stl file sizes of approximately 30GB. Samples were printed overnight (approximately 8 hours printing time per model; Figure 3J) to produce high resolution scale (x2000) replicas of each species of pollen grain (Figures 3K,L & 4F).

Human Erythrocyte

Confocal visualisation of human blood smears revealed a strong autofluorescent signature from erythrocytes in both the green and red range of the visible spectrum. As the cells were closely associated, we employed a circular ROI (region of interest) to delineate a scan area around individual erythrocytes. Confocal Z-stacks through the cells showed a disc diameter of approximately 8 micrometres and a minimum thickness at the centre of <1 micrometre, in agreement with the known dimensions of these cells. Surface rendered 3D reconstructions showed the characteristic biconcave morphology of the erythrocyte (Figure 5A). Prior to the 3D printing process a clipping plane was introduced through the erythrocyte disc diameter so that the model could be printed in two halves in order to convey the biconcave discal morphology evident in histological section planes (Figure 5B-C).

Earthworm Leukocyte (chloragocyte)

Chloragocytes obtained from the coelomic cavity of the earthworm (Eisenia fetida) were highly autofluorescent across the visible range. A strong autofluorescent signal derived from flavin-rich intracellular organelles, or chloragosomes [18], with a weaker cytoplasmic autofluorescent component (Figure 5D). Segmentation of grey values of cellular autofluorescence allowed surface rendering of both the strong flavin signal from the chloragosomes, which were modelled in green, in addition to the weakly autofluorescent cytoplasm, which was modelled in red (Figure 5E). Furthermore, a clipping plane was introduced equatorially into the 3D model with an offset between red and green channels to expose internal surfaces and reveal topographic detail of the chloragosomes in the final 3D print (Figures 5E-F).

Plant Root

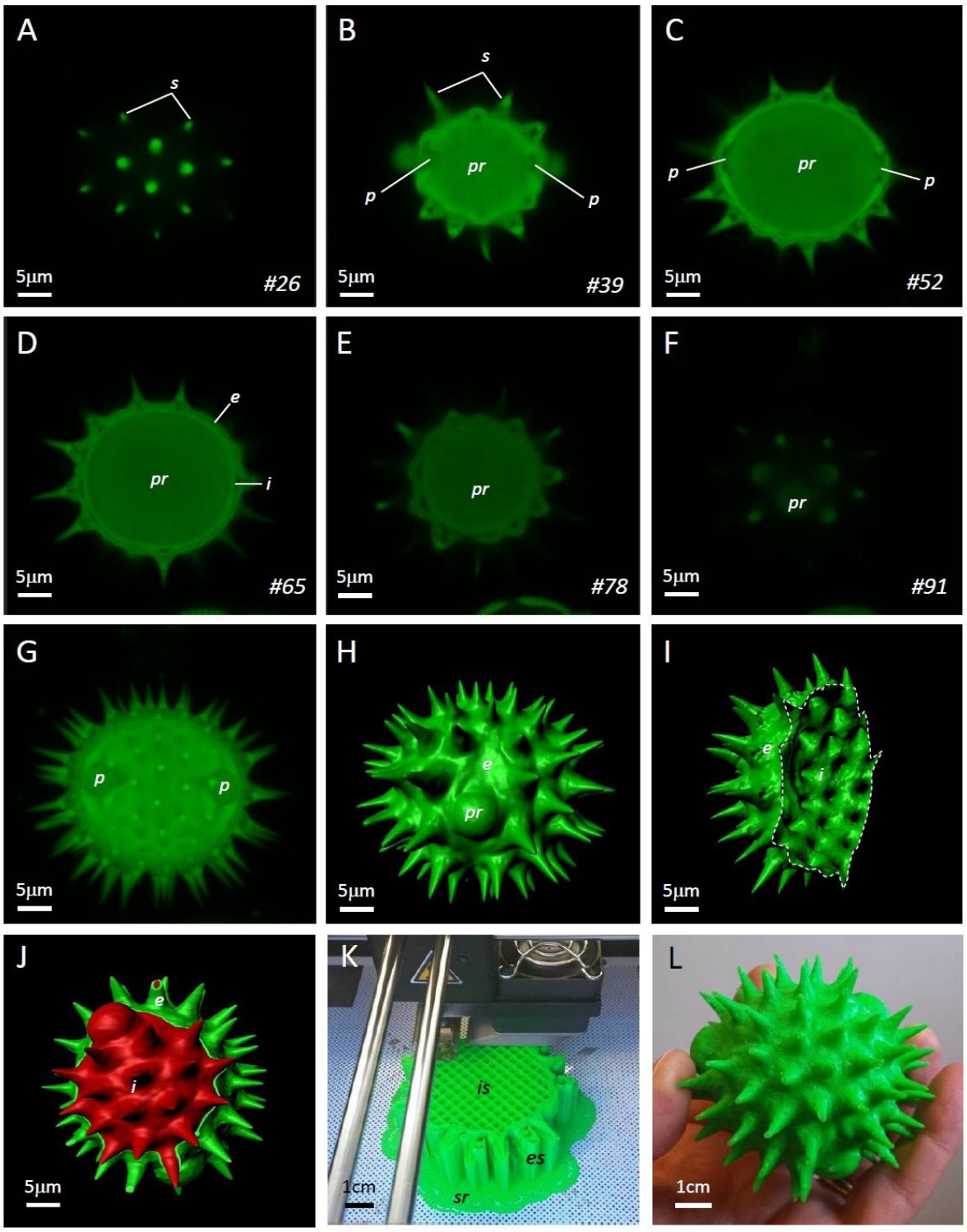

Figure 3. Sequence of steps showing the generation of a 3D printed model of a pollen grain from the common Daisy (Bellis perennis).
A-F. Selected optical sections (A, #26; B, #39; C, #52; D, #65; E, #78; F, #91) from Z-stack through pollen grain comprising 112 sections. Note spiny ornamentation (s) of outer exine (e) layer. An internal sheath, or intine (i), surrounds the protoplasm (pr). Distinct pores (p) allow shrinkage and swelling of the pollen grain and serve as an exit for its protoplasmic contents.
G. Maximum intensity 3D projection produced from the Z-stack.
H. Surface-rendered model showing outer structure of the exine.
I. Cut plane model showing internal surface structure of intine (dashed line indicates clipping plane).
J. 3D rendered internal surface (red) following image segmentation
K. 3D printing of the surface-rendered model. Note internal and external support scaffolds (is and es respectively) and underlying support raft (sr). The external supports are detached after printing.
L. The finished 3D printed model showing outer surface structure of the pollen grain. Scale bars denote sample dimensions.

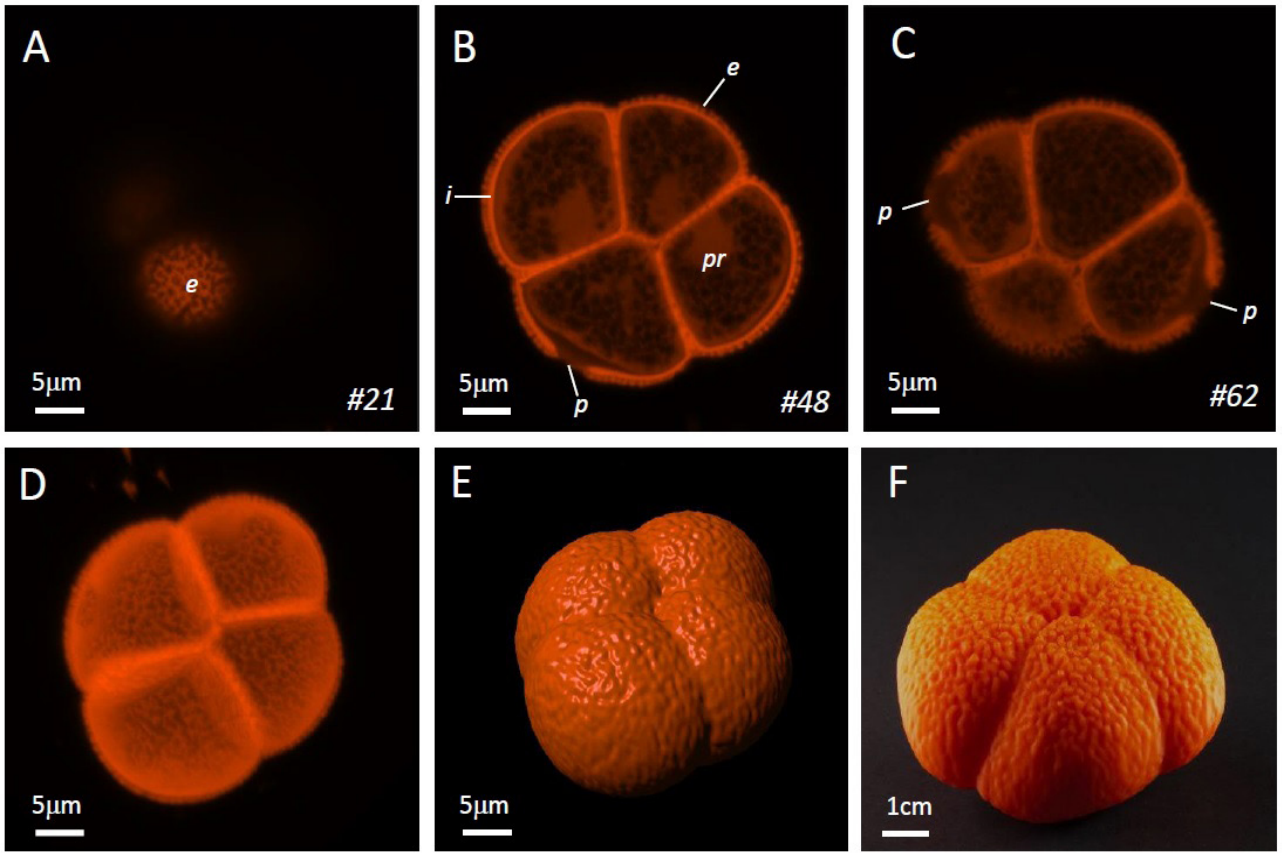

Figure 4. Generation of a 3D print of Bulrush (Typha latifolia) pollen.
A-C. Selected optical sections (A, #21, B, #48, C, #62) from a confocal Z-stack comprising 86 sections. Grains from this species are arranged into tetrads with reticulate patterning of their exine (e). The protoplasm (pr) is enclosed by intine (i), apart from at distinct pores (p) within the wall.
D. Maximum intensity projection showing internal and external structure.
E. Surface rendered model.
F. Resultant 3D print of pollen. Scale bars denote sample dimensions.

Epifluorescent observation of a transverse histological section through the rhizome of a Lilly of the Valley plant *(Convallaria majalis)* revealed strong autofluorescence across the visible spectrum. The green autofluorescent signal from the cellulose-rich cell walls and lignified vascular channels was used to generate Z-stacks of optical sections through the tissue. Maximum intensity projections and surface renders revealed the 3D structural organisation of the concentric vascular channels, comprising xylem and phloem elements, and surrounding parenchyma tissue (Figure 5G-H). This complex internal architecture was faithfully replicated at high resolution in the 3D printed model (Figure 5I).

Insect Compound Eye

Optical sections taken of blue/green autofluorescence through the compound eye of an ant (Myrmica rubra) revealed the tight, 3D structural organisation of the constituent hexagonal visual units, or ommatidia, in both maximum intensity and surface rendered reconstructions (Figure 5J-K). Confocal reflectance imaging after sputter coating the sample with gold provided a similar level of surface detail of the ommatidia (Figure 5L) and could be used as an alternative method for generation of 3D prints. Surface detail of the compound eye was reproduced at high fidelity in the resultant 3D print (Figure 5M).

Zebrafish Larva (1dpf; Prim-5)

Lightsheet microscopy of Zebrafish larvae (Danio rerio; 1dpf; Prim-5) fluorescently labelled with FITC-phalloidin for F-actin and DAPI for nuclear context, provided exquisite detail of both surface and internal structure. Maximum intensity reconstructions (Figure 6A,B) of this early developmental stage, showed the larvae to be approximately 2mm in length, comprising head, trunk and tail, arched around the yolk sac. The developing eyes and brain were visible, as were some axial structures of the spine including neural tube, notochord, the somites and their boundaries. The topography of these internal structures was manifest in the surface-rendered models (Figure 6C D) and faithfully replicated in the resultant 3D print (Figure 6E).

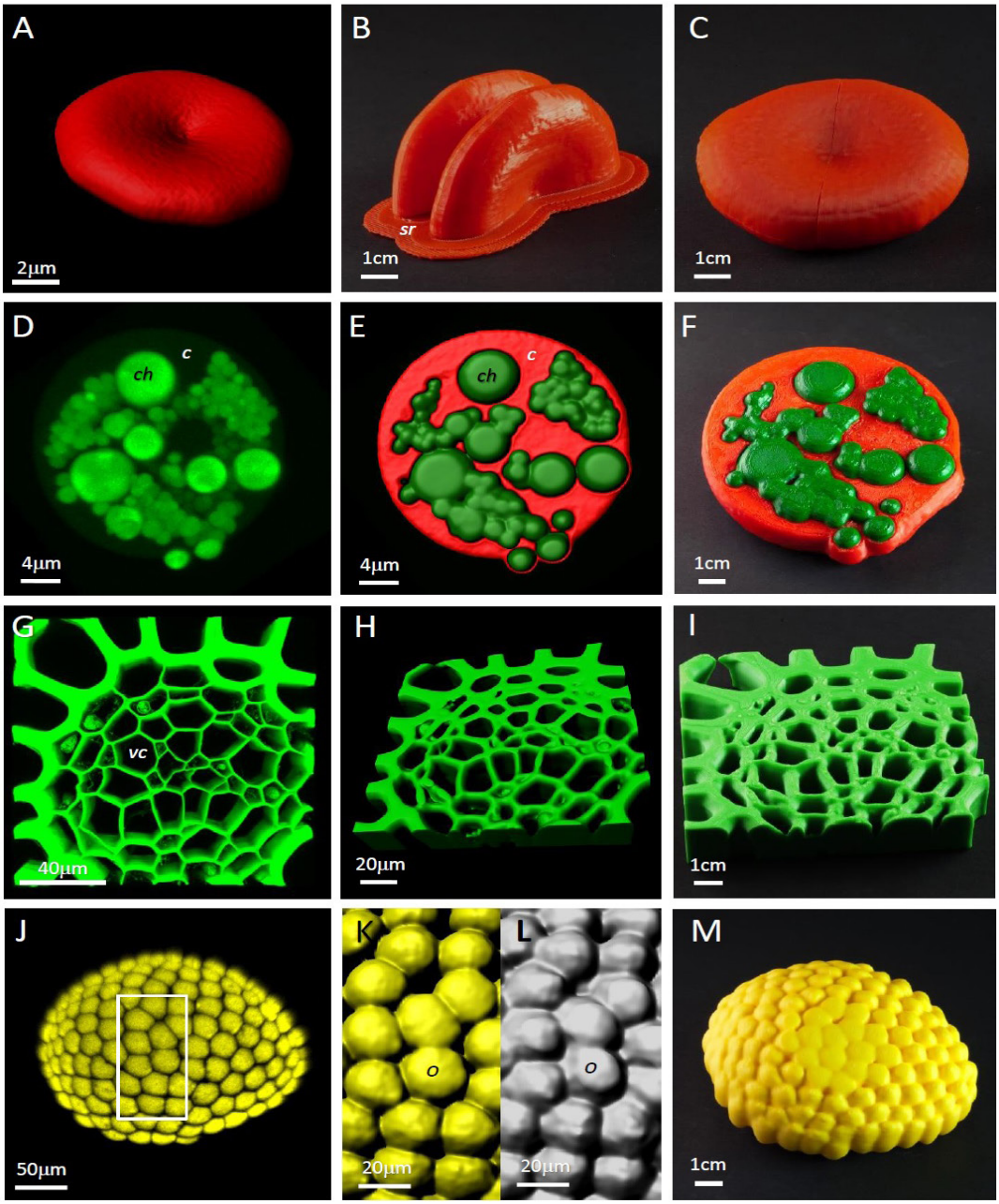

Figure 5. Reconstruction of confocal volume data sets for 3D printing. A-C. 3D modelling of a human red blood cell.
A. Surface-rendered model of the erythrocyte generated from a confocal Z-stack comprising 11 sections.
B. The erythrocyte model was printed in two halves to convey the characteristic biconcave morphology visible in histological section planes. The support raft (sr) is still attached in this figure.
C. The completed 3D print of the erythrocyte.
D-F. 3D reconstruction of an eleocyte (chloragocyte) from the earthworm (Eisenia fetida).
D. Maximum intensity reconstruction of the cell generated from a stack of 9 sections. Note highly autofluorescent, flavin-rich chloragosomes (ch).
E. Surface rendered model showing internal structure of the chloragocyte. Grey values of cellular autofluorescence were used to segment the strong flavin signal from the chloragosomes (ch; depicted in green) from the weakly autofluorescent cytoplasm (c, depicted in red). An equatorial clipping plane was introduced into the model with an offset between red and green channels to expose the surface topography of the chloragosomes.
F. The finished 3D print showing internal structure of the chloragocyte. Chloragosomes have been contrasted with green acrylic.
G-I. 3D reconstruction of plant root tissue from Lilly of the Valley (Convallaria majalis).
G. Maximum intensity reconstruction of the root generated from a confocal Z-stack comprising 64 sections. The vascular canals (vc) and chloroplasts (c) within associated root cells are visible.
H. Surface-rendered model of the root tissue. The model has been tilted on its vertical axis to highlight sample thickness.
I. The finished 3D print of the rhizome. J-L. 3D reconstruction of the compound eye of the common garden ant (Myrmica rubra).
J. Maximum intensity projection of the eye generated from a confocal z-stack comprising 40 sections. Boxed area is shown in detail in K.
K-L. Surface-rendered images generated from (K) autofluorescence- and (L) reflectance-based image data showing detail of the individual optical units, or ommatidia (o) making up the insect's compound eye.
M. The finished 3D printed model of the compound eye (generated from the autofluorescent signal). Scale bars denote sample dimensions.

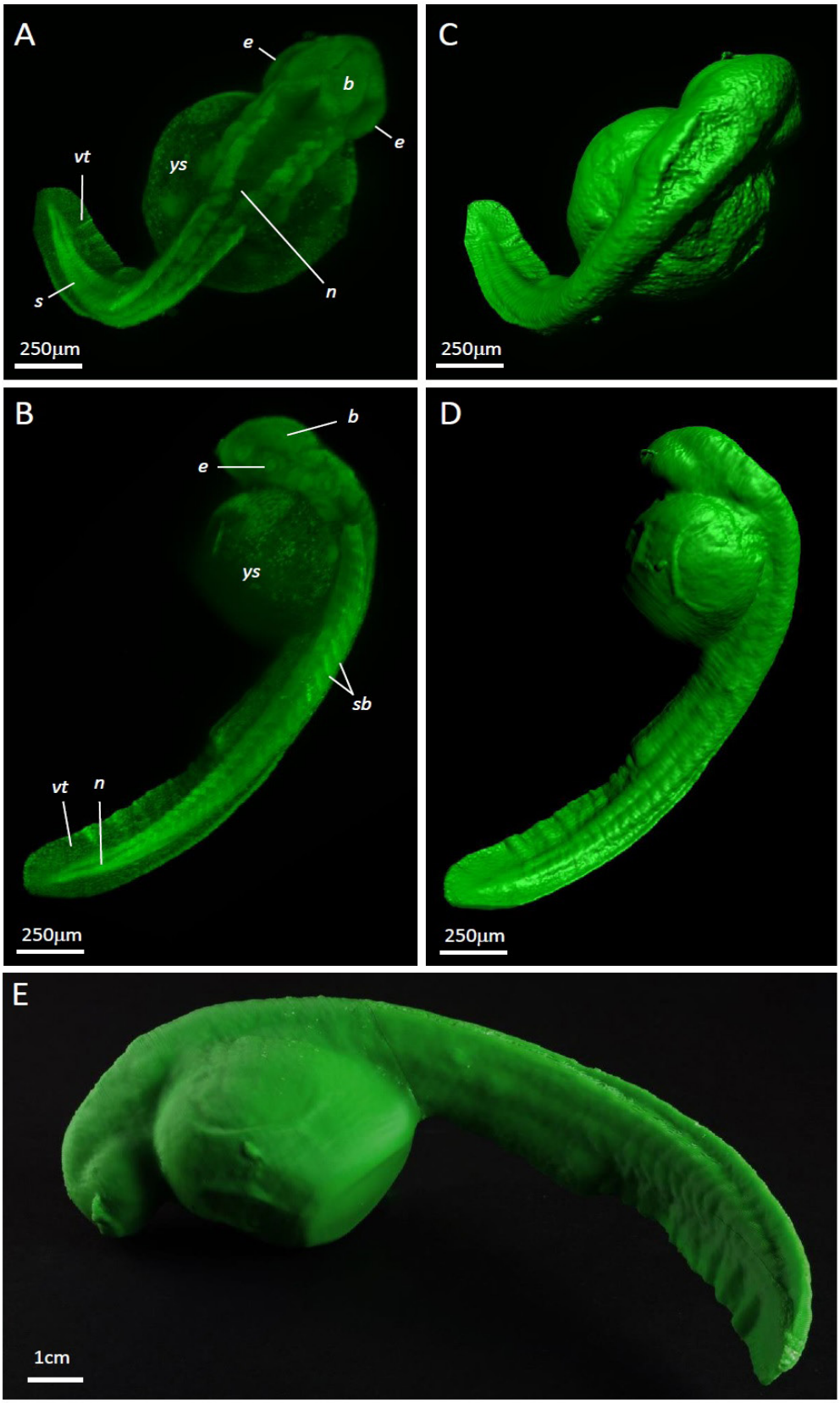

Figure 6. Generation of a 3D printed model of a developing Zebrafish larva (1dpf).

A-D. 3D reconstruction of the lightsheet volume dataset comprising 1650 optical sections. Dorsal (A,C) and lateral (B,D) views of the larva are depicted as maximum intensity (A,B) and surface-rendered (C,D) 3D models. b, brain; e, eye; n, notochord; s; somite; sb, somite boundaries; vt, ventral tail; ys, yolk sac. E. Finished 3D print of Zebrafish larva. Scale bars denote sample dimensions.

Discussion

This paper describes methodology for the generation of scale 3D replicas of biological samples from multi-format microscope volume datasets for use in science engagement and teaching applications using affordable, entry-level FFF 3D printing technology. Whilst we have used confocal and light-sheet systems to generate the 3D models, in principal the technique can be utilised with any imaging platform that generates volume datasets through optical sectioning. Using the methodology described, 3D prints can be generated from fluorescence- or reflectance-based imaging modalities, utilising cell/tissue autofluorescence, targeted fluorochromes/fluorescent proteins, or by sputter coating of samples by physical vapour deposition with gold to generate a reflective surface. The technique can also be exploited to physically model both the external and internal surfaces of the sample by introducing X,Y & Z clipping planes into the surface-rendered digital mesh. This approach would therefore be useful for intracellular modelling of multi-channel fluorescence (either from targeted probes or autofluorescent peaks) or by image segmentation post-acquisition, either through grey value thresholding or via a filter-based segmentation algorithm [19].

In this study we have utilised high-end image analysis software (Bitplane Imaris, Oxford Instruments) to generate the surface-rendered 3D meshes; however, free, open source software; e.g. the Image J plugin bundle, Fiji (https://fiji.sc/ ; [20]) provides a similar toolset that will allow the generation of .stl files from surface-rendered Z-stacks from all major microscope image formats. Excluding imaging costs, the actual outlay for generating the FFF 3D prints described in this study is therefore minimal, with a typical cost of around £10-£15 per model of around 10cm^3 including finishing and with printing times of around 8 hours. The methodology described can also be applied to other higher resolution 3D fabrication procedures (e.g. SLA and SLS) that are compatible with the .stl file format used here. Furthermore, the 3D prints can be used as masters to generate moulds that would allow rapid bulk casting of the models or permit the use of novel fabrication materials.

The 3D prints generated using the procedures outlined in this paper have significant advantages over both 2D representations, e.g. micrographs, and 3D reconstructions rendered *in silico*. Critically, they can be examined by hand, thus presenting haptic as well as visual cues about structure and therefore function [20]. This is significant, as our brains decode complex spatial information in our environment through multi-sensory integration, not just through sight. As well as providing complementary tactile information about microscopic specimens, we have also found the models to be invaluable in stimulating scientific engagement through inquiry, discussion and experience sharing - central tenets of teaching and learning. They therefore have significant utility in pedagogy and kinaesthetic learning, with clear benefits for visually impaired individuals or those with other physical or learning difficulties [22,23]. The workflow described in this paper also has considerable relevance to STEM education, a priority area of education identified as being of utmost importance to society, as it encompasses and integrates a variety of overlapping themes and technologies within the fields of science, technology, engineering and maths. It is therefore used in our undergraduate teaching and training programmes and for science outreach and engagement activities.

The potential of 3D printing to convey meaningful scientific information about microscopic structure and function in science education and research is slowly becoming realised. A small number of recent studies have implemented additive manufacturing techniques to generate physical models from microscope volume datasets [8-11]. Of note, [9] have developed a lab-based teaching method to generate 3D prints of skeletal muscle cells from confocal datasets; whereas both [8,10] describe fabrication approaches to generate physical models from optical image data. Whilst our general workflow is broadly similar to these studies, by applying a variety of sample contrast techniques, different optical imaging modalities and 3D reconstruction methods, we provide additional, complementary procedures that greatly extend the methodology.

Additive manufacturing is still an evolving technology and whilst its advantages are considerable, it has some notable disadvantages which include print reliability, resolution, size, speed and time. The FFF 3D printer that was used in this study proved extremely reliable (with a failure rate as low as 1-2% in our hands); however, it is not uncommon to experience poor quality prints or print failure resulting from clogged printing nozzles, filament misfeeds, poor adhesion of the print raft to the heated print bed, and other technical issues associated with this format. In this study we applied a print resolution of 140 microns with low infill to provide an acceptable compromise between resolution and speed (100mm/s) with print times of approximately 8 hours. Whilst this kept layering artefacts to an acceptable level, there was an obvious loss of resolution in the final 3D print relative to the original microscope dataset. However, it is worthwhile noting that greyscale thresholding, required to generate the surface rendered model for 3D printing, would also obscure some fine detail. A further loss of detail occurs downstream following removal of the print scaffold, which leaves minor imperfections on the surface of the 3D print that require physical smoothing, also adding to the processing time. A final limitation is the size of the 3D build chamber which determines the overall size of the 3D print; thus in this study, models larger than a workfield volume of 200 x 200 x 180mm (e.g. the Zebrafish larva) had to be printed as two halves and then subsequently fused together.

Despite these limitations, ongoing technological progress is delivering measurable improvements in additive manufacturing. Newer, more affordable FFF printers with large build areas can print at higher resolution (<25 micrometres) in

two colours or with different printing materials (e.g. resin, plastic, metal). Dual extrusion printers that can generate 3D prints with water-soluble polyvinyl alcohol (PVA) scaffolds [24] allow more complex structures to be printed at higher fidelity and requiring significantly less manual finishing, further reducing costs. The cost of the printers themselves and their printing materials has also tumbled, now making them viable standard laboratory acquisitions. It is anticipated that these developments will increase the accessibility of 3D printing as a transformative technology and, in the current context, facilitate greater understanding and appreciation of the microscopic world.

Author Contribution:
Perry I, Szeto J-Y contributed equally to this work.

Acknowledgements

Thanks to Dr Emyr Lloyd Evans and Dr Luke Haslett, Cardiff School of Biosciences, for providing the Zebrafish samples for Lightsheet microscopy. Thanks also to Professor Peter Kille and Dr Carsten Muller for providing earthworm coelomocyte preparations as part of the Cardiff School of Biosciences Research Techniques module, BI2001. The Zeiss LSM880 Airyscan confocal microscope, Zeiss Lightsheet Z.1 microscope and Bitplane Imaris 3D workstation were all purchased through generous support from Cardiff University's Research Infrastructure fund.

References

1. Stansbury JW, Idacavage MJ. 3D printing with polymers: challenges among expanding options and opportunities. Dental Materials. 2016, 32(1): 54-64.

2. Campbell I, Bourell D, Gibson I. Additive manufacturing: rapid prototyping comes of age. Rapid Prototyping Journal. 2012, 18: 255-258.

3. Tack P, Victor J, Gemmel P, Annemans L.3D-printing techniques in a medical setting: a systematic literature review. Biomed. Eng. Online. 2016, 15(1): 115.

4. Rengier F, Mehndiratta A, von Tengg-Kobligk H, Zechman C.M, Unterhinninghoefen R et al. 3D printing based in imaging data: review of medical applications. Int. J. CARS. 2010, 5(4): 335-341.

5. McMenamin PG, Quayle MR, McHenry CR, Adams JW. The production of anatomical teaching resources using three-dimensional (3D) printing technology. Anat. Sci. Educ. 2014, 7(6): 479-486.

6. Da Veiga Beltrame E, Tyrwhitt-Drake J, Roy I, Shalaby R, Suckale J et al. 3D printing of biomolecular models for research and pedagogy. J. Vis. Exp. 2017, 121: doi:10.3791/55427.

7. Scalfani VF, Williams AJ, Tkachenko V, Karapetyan K, Pshenichov A et al. Programmatic conversion of crystal structures into 3D printable files using Jmol. J. Cheminformatics. 2016, 8: 66.

8. Cox BL, Schumacher N, Konieczny J, Reifschneider I, Mackie T.R et al. Fabrication approaches for the creation of physical models from microscopy data. 3D printing in Medicine. 2017, 3:2.

9. Bagley JR, Galpin AJ. Three-dimensional printing of human skeletal muscle cells: An interdisciplinary approach for studying biological systems. Biochem. Mol. Biol. Educ. 2015, 43(6): 403-407.

10. Paliwal, V, Hausch, P, Padmanabhan, V, Ramachandran R. Creation of a physical 3D homosapiens single-cell model using confocal microscopy data. FASEB J. 2013, 27: s764.2

11. Paliwal V, Konieczny J, Eliceiri K, Reifschneider I. Creation of cell models from confocal microscopy data files using rapid prototyping. FASEB J. 2010, 24: 517.

12. Ball AD, Job PA, Walker AEL. SEM-microphotogrammetry, a new take on an old method for generating high-resolution 3D models from SEM images. J. Micros. 2017; 267(2): 214-226.

13. Augusto I, Monteiro D, Girard-Dias W, Dos Santos TO, Rosa Belmonte et al. Virtual reconstruction and three-dimensional printing of blood cells as a tool in cell biology education. PLoS One. 2016, 11(8): e0161184.

14. Hughes L. 3D printing for biological electron microscopy. Microscopy and Analysis. 2015, 138: 14-18.

15. Flood PM., Kelly R, Gutierrez-Heredia L. White Paper: Zeiss Lightsheet Z.1. Sample Preparation. 2013.

16. Berg R.H. Evaluation of spectral imaging for plant cell analysis. J. Micros. 2004, 214: 174-181.

17. Castro AJ, Rejón JD, Fendi M, Jiménez-Quesada MJ, Zafra A et al. Taxonomical discrimination of pollen grains by using confocal laser scanning microscopy (CLSM) imaging of autofluorescence. In: Microscopy: Science, Technology, Applications and Education, Edition. 2010, Chapter: 13, 607-613.

18. Koziol B, Markowicz M, Kruk J, Plytycz B. Riboflavin as a source of autofluorescence in Eisenia fetida coelomocytes. Photochem. Photobiol. 2016, 82(2): 570-573.

19. Roysam B, Lin G, Abdul-Karim M-A, Al-Kofahi O, Al-Kofahi K et al. Automated three-dimensional image analysis methods for confocal microscopy. In: Pawley, J (ed) Handbook of biological confocal microscopy. Third Edition. Springer Sci-

ence & Business Media, LLC, N.Y. 2006, Chapter 15, 316-337.

20. Schindelin J Arganda-Carreras I, Frise E, Kaynig V, Longair M et al. Fiji: an open-source platform for biological-image analysis. Nature Methods. 2012, 9(7): 676-682.

21. Sato M. A haptic virtual environment for molecular chemistry education. In: Pan Z, Cheok, DAD., Muller W, El Rhalibi, A. (eds) Transactions on Edutainment I. LNCS Springer, Heidelberg. 2008, 5080: 28-39.

22. Kolitsky MA. 3D printed tactile learning objects: proof of concept. J Blindness Innovation and Research. 2014, 4 (1).

23. Kolitsky MA, Reshaping teaching and learning with 3D printing technologies. e-mentor. 2014, 4: 84-94.

24. Duran C, Subbian V, Giovanetti MT, Simkins JR, Bayette FR. Experimental desktop 3D printing using dual extrusion and water-soluble polyvinyl alcohol. Rapid Prototyping Journal. 2015, 21: 528-534.